



## A Multiscale Model for Electrochemical Reactions in LSCF Based Solid Oxide Cells

Linjian Ma, Pikee Priya,  and N. R. Aluru<sup>z</sup>

Department of Mechanical Science and Engineering, Beckman Institute for Advanced Science and Technology, University of Illinois at Urbana-Champaign, Urbana, Illinois 61801, USA

Lanthanum Strontium Cobalt Ferrite ( $\text{La}_{1-x}\text{Sr}_x\text{Co}_{1-y}\text{Fe}_y\text{O}_{3-\delta}$  or LSCF), a mixed ionic-electronic conductor is widely used as an electrode in solid oxide cells (SOCs). The reactions and transport at this oxygen electrode are complex and distributed across several length and time scales. However, a comprehensive computational model that could provide accurate and reliable linkages between different scales to predict the electrochemical characteristics of these electrodes is missing. Here, we develop a multiscale model combining density functional theory calculations, transition state theory and continuum modeling for the oxygen-based reactions at the cathode/anode in LSCF based solid oxide fuel cells (SOFC)/electrolysis cells (SOEC), to elucidate the critical reaction steps and predict the performance of the device. Density functional theory calculations were used to obtain the free energy barriers for different reaction steps while transition state theory was used to predict the reaction rate constants/diffusivities for each step based on the free energy barriers. The continuum theory utilized these reaction rate constants and diffusivities to obtain the overpotential-current density relations. The proposed multiscale model yields a quantitative agreement with the overpotential-current density data from experiments. The results indicate that oxygen exchange at the LSCF surface, rather than the triple-phase boundary, is the main contributing reaction pathway for a single phase LSCF electrode. For the entire cathodic and anodic reaction pathway, the reaction step involving the splitting of the surface peroxo units into oxo units under SOFC mode or the combination of surface oxo units into peroxo units under SOEC mode is the rate-limiting reaction step, and the diffusion of oxide ions in bulk LSCF is the rate-limiting diffusion step. We also predict that the SrO terminated LSCF surface is not an efficient surface structure for oxide ion diffusion.  
© 2018 The Electrochemical Society. [DOI: [10.1149/2.0921814jes](https://doi.org/10.1149/2.0921814jes)]

Manuscript submitted July 18, 2018; revised manuscript received October 3, 2018. Published November 6, 2018.

Hydrogen is a clean and sustainable fuel compared to fossil fuels such as coal and petroleum, as it does not produce harmful gases and could be generated through water electrolysis.<sup>1</sup> Developing efficient and environment-friendly processes to utilize as well as to generate hydrogen is of great interest owing to its renewability. Solid oxide cells (SOCs) are high-efficiency energy conversion devices for generation of electricity or production of hydrogen at high temperatures.<sup>2</sup> They can work in a fuel cell mode (SOFC) to transform hydrogen and oxygen to steam and produce electricity,<sup>3-5</sup> or in electrolysis cell mode (SOEC) to consume electricity and produce hydrogen from water.<sup>1,6,7</sup> SOCs have attracted wide attention, and a lot of research has been dedicated to this field in recent times.

Typical solid oxide cells have three components, one dense electrolyte, and two porous electrodes. Stable oxide ion conductors, such as Ytria-Stabilized Zirconia (YSZ) and Strontium Magnesium doped Lanthanum Gallate (LSGM), are generally used as electrolytes<sup>5,7-9</sup> due to their high ionic conductivity. Transition metals, such as Pt and Ni, are widely used as the hydrogen electrodes. Mixed Ionic Electronic Conductors (MIEC) such as  $\text{La}_{1-x}\text{Sr}_x\text{Co}_y\text{Fe}_{1-y}\text{O}_{3-\delta}$  (LSCF)<sup>5,10</sup> are typically used as the oxygen electrodes due to their high catalytic activity. To build an efficient SOC, the electrical resistance of the entire cell should be small. Usually, the oxygen electrode polarization resistance is high and is a primary impediment to high cell efficiency.<sup>5,11,12</sup>

The reactions at the oxygen electrode in Kroger-Vink notation are  $0.5\text{O}_2 + 2e' \rightarrow \text{O}_o''$  in SOFC and  $\text{O}_o'' \rightarrow 0.5\text{O}_2 + 2e'$  in SOEC mode. The high polarization resistance in the oxygen electrode is due to the slow reaction rates of these cathodic/anodic reactions. To lower the resistance, MIECs are used as oxygen electrodes, as oxygen release or incorporation can be extended to the entire electrode surface rather than only near the triple-phase boundaries (TPB). LSCF, a typical MIEC material, is a p-type semiconductor with electronic and ionic conductivity.<sup>13</sup> It is widely used as an oxygen electrode because of its high stability, good catalytic ability for oxygen reactions and high oxide ion conductivity.<sup>14-16</sup> Understanding the reaction mechanisms at the LSCF based oxygen electrode is essential for designing energy efficient SOCs.

Many computational and experimental studies have been conducted in the past to investigate the reaction mechanisms in LSCF based electrodes. Electrochemical characteristic curves and overall

reaction rates have been obtained through experiments,<sup>17-19</sup> but computational studies are necessary to gain detailed insights into the reaction pathways involved. First principle calculations, including density functional theory (DFT) and ab initio molecular dynamics (AIMD), can provide detailed insights into the chemical reactions occurring at the electrode during operation.<sup>16,20-24</sup> However, the high computational cost restricts the system to fewer than 200 atoms, which is inadequate to mimic transport across the entire length of the cell, requiring continuum scale methods. Much work has been done on understanding the reaction steps using continuum simulations.<sup>13,25,26</sup> In one of the initial efforts, Adler, Lane, and Steele developed a continuum model to explain the oxygen reduction mechanisms in MIEC.<sup>25</sup> They defined a parameter 'penetration depth',  $\delta$  which was critical in determining whether oxygen exchange is confined to the TPB or extends to the surface area of the electrode. Later, to determine the rate-limiting reaction step for a MIEC electrode surface, Fleig evaluated the current-voltage relations with electron transfer and ion transfer as the rate-limiting steps.<sup>27</sup> In a more recent work, Yurkiv et al. developed a model to predict impedance spectra of a MIEC electrode which were consistent with experiments.<sup>26</sup> However, oxygen ion transport and change of ion/vacancy concentrations across the cathode were not considered which could affect the chemical capacitance. While these studies have provided critical insights into the reaction mechanisms and rate-limiting steps in LSCF electrodes, the fitted values for critical physical parameters, such as reaction rate constants and diffusivities, used in the continuum models lower their reliability. The details of the mechanisms in the reaction pathways are also missing. Therefore, it is essential to build an accurate model incorporating all the underlying electrochemical phenomena using realistic values for various physical parameters for all the sub-processes involved.

In this work, we develop a multiscale approach combining DFT-based quantum scale calculations, transition state theory, and continuum scale simulations to determine the key reaction steps in an LSCF-based electrode. First, DFT+U calculations are performed to calculate the energy barriers for each reaction step and the vibrational frequencies of atoms, to obtain the free energy landscape of the entire reaction pathway. These results are used in the transition state theory to get the reaction rate constants and diffusivities. The calculated parameters are subsequently used in the continuum scale to calculate the current density-overpotential curves which are compared with experimental data. We also investigate the sensitivity of the current density-overpotential curves to reaction rate parameters

<sup>z</sup>E-mail: [aluru@illinois.edu](mailto:aluru@illinois.edu)

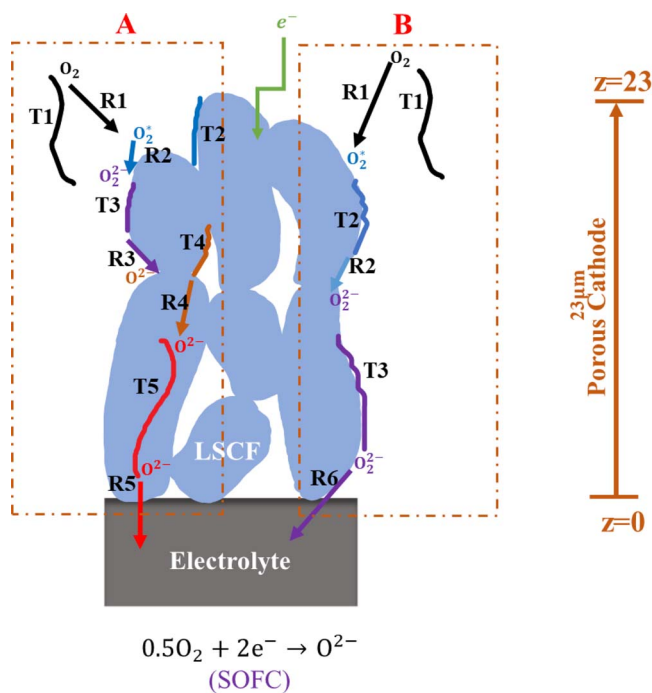


**Figure 1.** Schematic representation of the reactive pathways in the model (presented in SOFC mode). The blue grains are the LSCF phase, the white spaces between them are the gas phase, and the gray rectangle is the dense electrolyte phase (GDC). Oxygen molecules can transport into the electrolyte through the bulk LSCF phase, which is shown in the left part of the figure denoted by path A, or through the TPB, which is shown in the right part of the figure denoted by path B. The reactive pathways under SOEC mode are the reverse process of that for SOFC.

to determine the key reaction steps. Such a multiscale framework is unique and provides for the critical linkages between the physics at different length scales and can easily be extended to other material systems minimizing the need for rigorous experiments.

### Methods and Computational Details

#### Model structure, reaction steps, and multiscale framework.—

The model system used in the current work is shown in Fig. 1. It consists of a porous, 23  $\mu\text{m}$  thick  $\text{La}_{0.6}\text{Sr}_{0.4}\text{Co}_{0.2}\text{Fe}_{0.8}\text{O}_{3-\delta}$  (LSCF) electrode and a dense Gadolinium-doped Ceria (GDC) electrolyte. The upper boundary of the electrode is exposed to the pure oxygen gas under 1 atm pressure and the lower boundary interfaces with the electrolyte. All the reactions are considered at an operating temperature of 1073 K, as used in validation experiments.<sup>13</sup>

The electrochemical processes (reactions and transport) considered in the present study, for LSCF-based SOFC are shown in Fig. 1. The SOEC mode reactions are the reverse of those shown for the SOFC mode. The entire oxygen reduction process can be sub-divided into five transport steps (T1 to T5) and six reaction steps (R1 to R6). Details on these steps are presented in Section S1 of the Supporting Information. It should be noted that oxygen can transport into the electrolyte through both LSCF/GDC interface and the triple-phase boundary as denoted by paths A and B, respectively, in Fig. 1. The contribution to overall current from the two pathways is discussed later.

The overall multiscale framework connecting the physics at atomistic (DFT+U calculations), meso (Transition state theory) and continuum (Continuum modeling) scales, is presented in Fig. 2 and is discussed in more detail in the following sections.

**DFT+U calculations.**—Vienna Ab initio simulation package (VASP),<sup>28–30</sup> version 5.3.5 was used to perform all spin-polarized DFT+U calculations with periodic boundary conditions.<sup>31–33</sup> Generalized gradient approximation (GGA) exchange–correlation functional of Perdew–Burke–Ernzerhof (PBE)<sup>34</sup> was used, and the conjugate-gradient method was utilized to optimize the ionic positions until the Hellmann–Feynman forces on each ion were less than 0.04 eV/Å. The energy convergence criterion was  $10^{-5}$  eV. The plane wave basis set cutoff energy was set to be 500 eV. The projector augmented wave (PAW) method was used to calculate the interactions between valence electrons and nuclei plus core electrons.<sup>35,36</sup> The PAW potentials with valence configurations of La ( $5s^25p^66s^25d^1$ ), Sr ( $4s^24p^65s^2$ ), Co ( $4s^24p^65s^2$ ), Fe ( $3d^84s^1$ ), O ( $2s^22p^4$ ), Ce ( $5s^25p^66s^25d^14f^1$ ) and Gd ( $5s^25p^66s^25d^14f^7$ ) were used.

The rotationally invariant formulation was used for the U terms to describe the electron–electron interactions in the 3d orbitals of Fe, Co atoms and 4f orbitals of Ce, Gd atoms.<sup>32</sup> In this formulation, only the differences ( $U_{\text{eff}}$ ) between the Coulomb (U) and exchange (J) values were the inputs of the calculations. The  $U_{\text{eff}}$  value for Fe, Co was chosen to be 4.0 eV,<sup>37–39</sup> and for Ce, Gd was chosen to be 5.0 eV,<sup>40</sup> which were recommended in the literature. The migration energy barriers and the transition state positions were calculated using the climbing image nudged elastic band method (CI-NEB).<sup>41</sup> Bader charge analysis was performed to estimate the atomic charges.<sup>42</sup> We used a  $4 \times 4 \times 4$  Monkhorst-Pack<sup>43</sup> k-point mesh for bulk systems and a  $4 \times 4 \times 1$  Monkhorst-Pack k-point mesh for free surface and interface systems.

$\text{La}_{0.6}\text{Sr}_{0.4}\text{Co}_{0.2}\text{Fe}_{0.8}\text{O}_{3-\delta}$  is the stoichiometry of the electrode material used in experiments.<sup>13</sup> To minimize the differences between the simulation structure and experimental stoichiometry, we focused on a similar structure  $\text{La}_{0.625}\text{Sr}_{0.375}\text{Co}_{0.25}\text{Fe}_{0.75}\text{O}_{3-\delta}$ . Such approximate structures have also been used in previous DFT studies on LSCF,<sup>16,39</sup> with physical and electrochemical properties matching experiments. The relaxed LSCF bulk structure used in the calculations is the supercell with  $2\sqrt{2} \times 2\sqrt{2} \times 2$  unit cells and is shown in Figs. 3a–3b. The

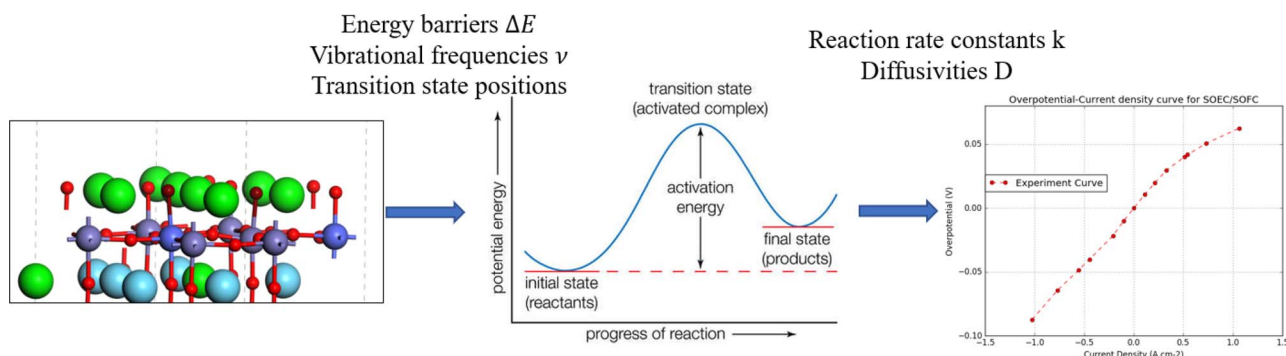


**Figure 2.** Schematic representation of the multiscale framework connecting different length scales. DFT+U calculations of the atomic structures give the energy diagram used by the transition state theory. The resulting kinetic parameters are then used in the continuum scale to predict the electrochemical characteristics.

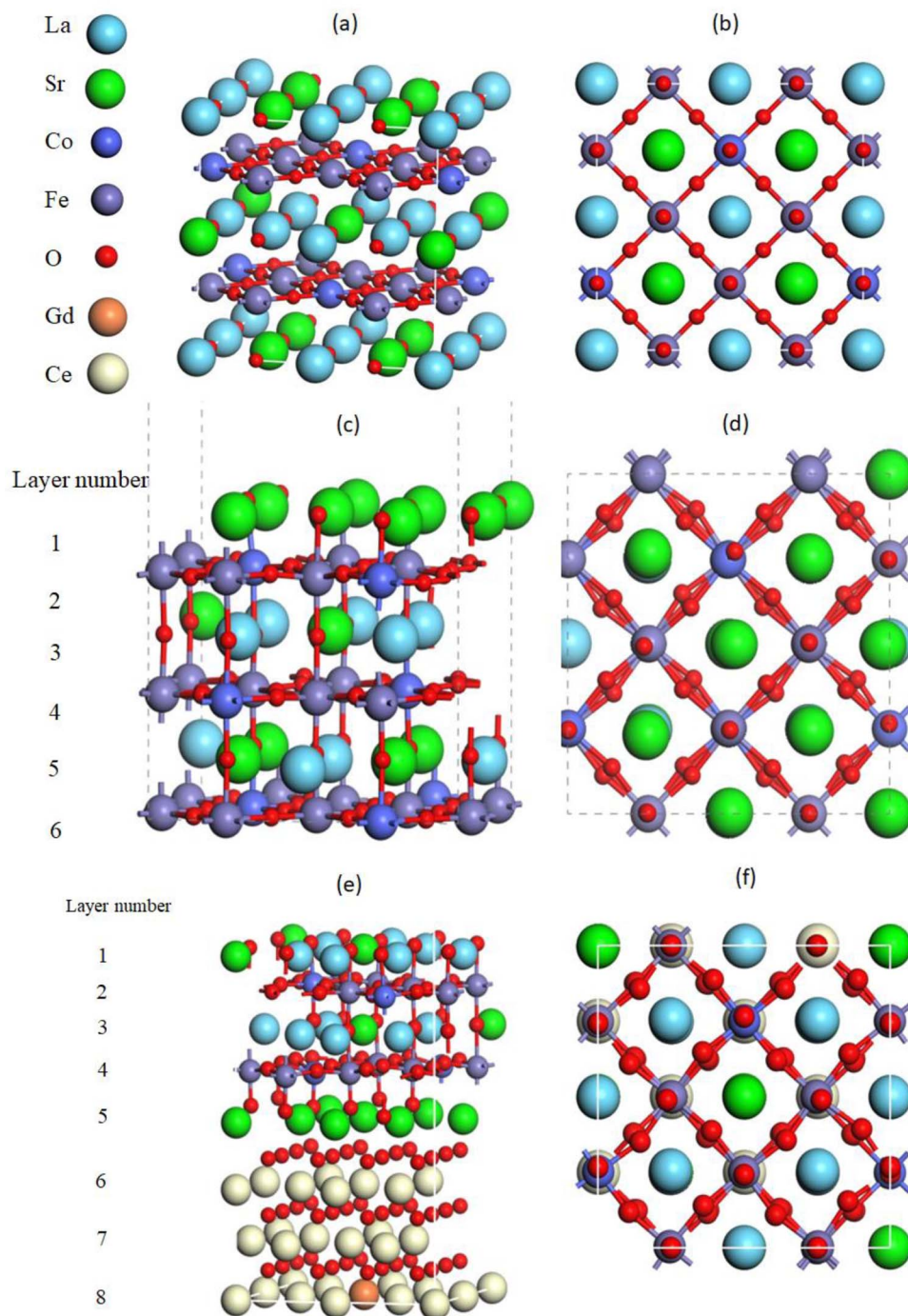


**Figure 3.** The structures used in the DFT+U calculations. The structures shown in the figures are after structural relaxations. (a-b) Side and top view of the LSCF bulk structure. (c-d) Side and top view of the LSCF surface structure. (e-f) Side and top view of the LSCF/GDC interface structure.

lattice parameters are  $a = b = c = 3.843 \text{ \AA}$  and  $\alpha = \beta = \gamma = 90^\circ$ , same as those in Reference 16. To confirm that the bulk LSCF structure is consistent with the normal  $ABO_3$  structure for perovskites ( $A = \text{La, Sr}$ ,  $B = \text{Co, Fe}$ ) and suitable for subsequent calculations, we calculated the vacancy formation energy in the structure using:

$$\Delta E_{f,vac} = E_{defect} + 0.5E_{O_2} - E_{host} \quad [1]$$

where  $\Delta E_{f,vac}$  is the vacancy formation energy,  $E_{defect}$  is the total energy of the bulk LSCF with one oxygen vacancy,  $E_{host}$  is the total energy of the perfect bulk LSCF, and  $E_{O_2}$  is the energy of an oxygen molecule.<sup>39</sup> The oxygen vacancy formation energies are calculated for

different positions in bulk LSCF and are found to be within the range of [0.95, 1.44] eV, consistent with previous experimental results.<sup>44–48</sup>

The LSCF free surface structure used in the calculations is shown in Figs. 3c–3d. An A-site terminated free surface rather than a B-site terminated free surface was chosen as it was experimentally observed through low energy ion scattering spectroscopy by Druce et al.<sup>49</sup> for LSCF although the B-site surfaces are catalytically more active. A (100) oriented 6-layer slab, was used here, as it is the stable surface in most perovskites.<sup>16</sup> A vacuum slab larger than 15 Å was used above the surface to minimize the interactions between the surface and its periodic images. The bottom layer atoms were fixed at the bulk position, while the rest of the atoms were fully relaxed. The

first, third and fifth layers are the AO layers, and the second, fourth and sixth layers are the BO<sub>2</sub> layers. Oxygen reactions at the LSCF electrode involve interaction with two vacancies which are also needed in the LSCF structure to maintain charge neutrality. Two different configurations have been considered, one with both the vacancies in the top SrO layer, and other with one vacancy in the SrO layer while the second in the lower Fe/CoO layer. The energetics for the two cases is also compared.

The LSCF/GDC interface structure used in the calculations is shown in Figs. 3e–3f. Here we used a (100) oriented 5-layer slab for LSCF phase, and a (100) oriented 3-layer slab for GDC phase. An approximate composition of Ce<sub>0.95</sub>Gd<sub>0.05</sub>O<sub>1.95</sub> has been used. For the size of the GDC layer chosen, the structure contains 1 Gd atom. A different configuration involving 2 Gd atoms with the Gd near the interface has also been considered. As LSCF and GDC have similar crystal structures and lattice parameters, the GDC structure is also chosen to be (100) oriented which can form a stable interface with (100) oriented LSCF. Discussion about other interface structures is presented in Section S2 of the Supporting Information. The lattice parameters for the interface structure are  $a = b = c = 3.834 \text{ \AA}$ , which are the mean lattice lengths for LSCF and GDC, and  $\alpha = \beta = \gamma = 90^\circ$ . As before, a vacuum slab larger than 15 Å was used. The bottom layer atoms were fixed at the bulk positions, the upper layer atoms were fixed at the bulk position along directions perpendicular to the slab, while the structure was fully relaxed. Due to the Sr segregation phenomenon at the interface which is commonly observed in the experiments,<sup>50–52</sup> the fifth atom layer, which is the interfacial layer between the two materials (shown in Fig. 3e), is chosen to be SrO layer.

**Transition state theory.**—Accurate parameter values for reaction rate constants and diffusivities are needed to perform continuum calculations. Some of them are already available in the existing literature, for example, diffusivities of O<sub>2</sub> in the gas phase and O''<sub>O</sub> in bulk LSCF,<sup>13,53,54</sup> while other parameters had to be calculated using transition state theory. The equations relating reaction rate constants and diffusivities to free energy barriers obtained from DFT+U calculations are as follows.

$$k = \frac{k_B T}{h} \exp\left(-\frac{\Delta G(T, C)}{k_B T}\right) \quad [2]$$

$$D = \frac{\chi^2 k_B T}{z} \exp\left(-\frac{\Delta G(T, C)}{k_B T}\right)$$

where  $k$  denotes the reaction rate constant,  $D$  denotes the diffusivity,  $k_B$  denotes the Boltzmann constant,  $T$  denotes the temperature,  $C$  denotes the concentration of different species,  $h$  denotes the Planck's constant, and  $G$  denotes the Gibbs free energy.

The free energy barriers are a function of temperature and concentration of species. Assuming that the influence of temperature and concentration on barriers are independent of each other, we have

$$\Delta G(T, C) = \Delta G(T) + \Delta G(C) \quad [3]$$

A discussion on the expressions for  $\Delta G(C)$  is provided in the Results and Discussion Section. The expressions for  $\Delta G(T)$  are available in the literature<sup>55–58</sup> and, additional details are presented in Section S3 of the Supporting Information.

**Continuum model.**—The entire oxygen reduction process has been subdivided into five transport steps and six reaction steps, as stated earlier. The continuum model used in the current work is a species transport model in 1D where the transient flux of a species is dependent on concentration gradients and electrical potential gradients (for charged species) taking care of source/sink for species through the surface/interface reactions.

The governing transport equation is as follows:

$$\frac{d}{dz} \left[ -\frac{\phi_l}{\tau_l} D_i \left( \frac{d}{dz} C_i - \frac{n_i F_a C_i}{RT} \frac{d}{dz} \varphi \right) \right] = s_i \quad [4]$$

**Table I. The source/sink terms and boundary conditions for concentration of various species in the continuum model.**

Place	Species	$s_i$	Top boundary condition	Bottom boundary condition
Gas phase	O <sub>2</sub>	$-r_{R1}$	$C = \frac{p}{RT}$	$\frac{d}{dz} C = 0$
LSCF surface	O <sub>2O</sub> <sup>x</sup>	$r_{R1} - r_{R2}$	$\frac{d}{dz} C = 0$	$\frac{d}{dz} C = 0$
	O'' <sub>2O</sub>	$r_{R2} - r_{R3}$	$\frac{d}{dz} C = 0$	$-D \frac{d}{dz} C = -r_{R6}$
	O' <sub>O</sub>	$2r_{R3} - r_{R4}$	$\frac{d}{dz} C = 0$	$-D \frac{d}{dz} C = r_{R6}$
Bulk LSCF	O'' <sub>O</sub>	$r_{R4}$	$\frac{d}{dz} C = 0$	$-D \frac{d}{dz} C = -r_{R5}$

where  $C_i$ ,  $D_i$ ,  $s_i$ ,  $n_i$  denotes the concentration, diffusivity, the source/sink term, and the ionic charge for the chemical species  $i$ , respectively.  $\varphi$  denotes the electric potential,  $\phi_l$ ,  $\tau_l$  denote the porosity and the tortuosity in phase  $l$ ,  $F_a$  denotes the Faraday's constant,  $T$  denotes the temperature, and  $R$  denotes the ideal gas constant. The expressions for the electric field,  $-\frac{d}{dz} \varphi$  are given in Section S4 of the Supporting Information. The expression for  $s_i$  is as follows:

$$s_i = \sum_{j=1}^{N_i} v_{j,i} r_j \quad [5]$$

$$r_j = k_j^+ \prod_{l=1}^{S_R} C_l^{-v_{j,l}} - k_j^- \prod_{l=1}^{S_P} C_l^{v_{j,l}} \quad [6]$$

where  $r_j$  is the reaction rate,  $v_{j,i}$ ,  $k_j^+$  and  $k_j^-$  are the stoichiometric factor of species  $i$  in reaction  $j$ , the forward and backward rate constants in reaction  $j$ , respectively,  $S_R$  and  $S_P$  are the number of reactants and products, and  $N_i$  is the number of reactions related to species  $i$ . Details about the expression of  $s_i$  for each species are in Table I.

The expression for current density is given by,

$$I = 2F_a (-r_{R5} - r_{R6}) \quad [7]$$

where  $r_{R5}$  is the reaction rate of R5, which is across the LSCF/GDC interface, and  $r_{R6}$  is the reaction rate of R6, across the TPB. The overall continuum model procedure is described in the flowchart in Fig. 4. The coupled equations are numerically solved using the finite volume method in OpenFOAM (Open Field Operation and Manipulation).<sup>59</sup>

## Results and Discussion

**DFT+U calculation results.**—The DFT+U calculations were performed for predicting the free energy profile for LSCF surface reactions, the free energy profile for LSCF/GDC interface reactions, and the free energy barrier for LSCF surface oxide ion diffusion. The detailed energy barrier values are presented in Table S6-1 and Table S6-2 in Section S6 of the Supporting Information. The optimized structures and additional details on these calculations are shown in Section S7 of the Supporting Information.

Fig. 5a shows the free energy profile for the LSCF surface reaction of oxygen reduction, O<sub>2</sub> + 4e' + 2V<sub>O</sub><sup>x</sup> → 2O''<sub>O</sub>. The entire process includes 4 sub-reactions, R1 (O<sub>2</sub> → O<sub>2O</sub><sup>x</sup>), R2 (O<sub>2O</sub><sup>x</sup> + V<sub>O</sub><sup>x</sup> + 2e' → O''<sub>2O</sub>), R3 (O''<sub>2O</sub> + V<sub>O</sub><sup>x</sup> → 2O'<sub>O</sub>) and R4 (which is transport of O'<sub>O</sub>). The charges on the O<sub>2O</sub><sup>x</sup>, O''<sub>2O</sub> and O'<sub>O</sub> have been predicted through bader charge analysis and have been found to be 0.34 e, 1.5 e and 1.2 e, respectively. The first sub-reaction, R1 is the adsorption of O<sub>2</sub> molecule (triplet spin state) on the LSCF surface to form an excited oxygen molecule, O<sub>2O</sub><sup>x</sup> in singlet spin state with an energy of binding  $E_b = 0.989 \text{ eV}$ . The bond length of this excited state is 1.26 Å which is more than that of a triplet state O<sub>2</sub> molecule of 1.20 Å. R2 is the attachment of the excited O<sub>2O</sub><sup>x</sup> molecule to a surface vacancy to form a peroxo species O''<sub>2O</sub>, also in singlet spin state. The  $E_b = 0.615 \text{ eV}$  and the O-O bond is further stretched to 1.472 Å, making it a very reactive species. For R3, the peroxo O''<sub>2O</sub> splits into two oxo species, O'<sub>O</sub> by attaching to a neighboring vacancy, V<sub>O</sub><sup>x</sup> (on surface SrO or sub-surface Fe/CoO layer). Calculations reveal that the energy of the structure containing V<sub>O</sub><sup>x</sup> next to a O''<sub>2O</sub> is 1.465 eV higher if the vacancy

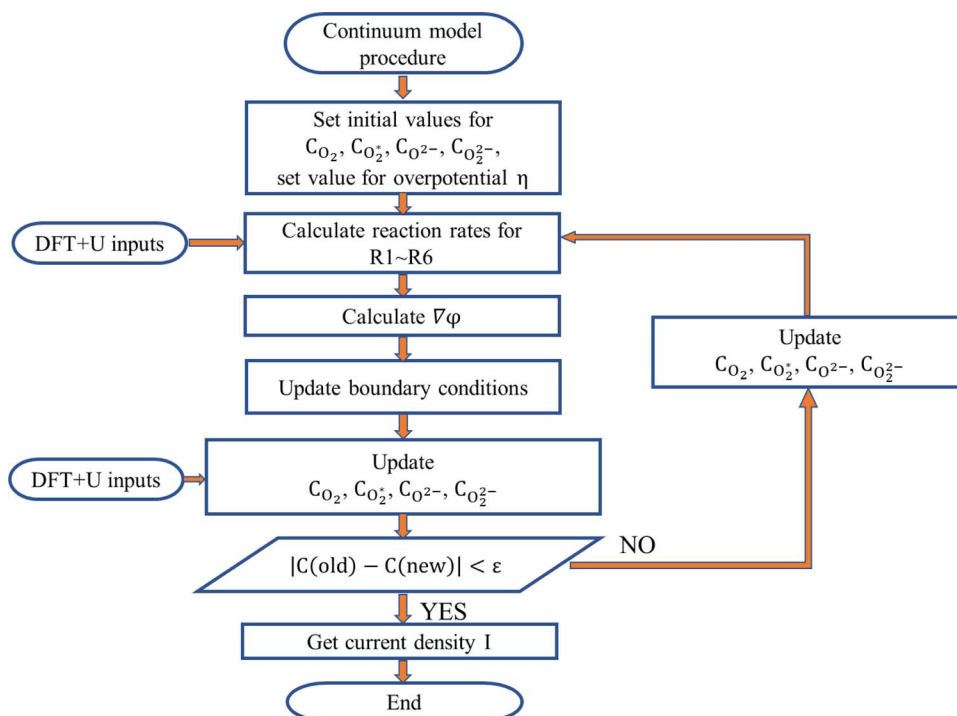


**Figure 4.** Flowchart summarizing the overall continuum model procedure.

is on the top SrO surface and 0.565 eV higher if the vacancy is in the lower Fe/CoO layer making the later configuration energetically more favorable. Also, the energy barrier for  $O_{2o}''$  split is 0.814 eV, and the barrier for combination of two  $O_o'$  is 2.343 eV for the vacancy in the top layer case which is more than 0.799 eV and 1.43 eV in the respective directions if the vacancy in the lower Fe/CoO layer case as seen in Figure 5a. These high barriers indicate that this process can be a rate-limiting step. R4 describes the process of  $O_o'$  transport to the bulk LSCF. From the calculations, it appears that the oxo species are less stable in the surface than in the bulk LSCF. This result is consistent with the literature, showing that surface vacancy segregation is an important phenomenon of LSCF.<sup>60</sup> It can be concluded that the largest barrier for the LSCF surface reactions comes from step R3, which contains the oxygen-oxygen bond breaking in SOFC mode or bond forming in SOEC mode. Besides, the  $V_o^x$  containing structure is a high energy configuration which also slows down the overall reaction rates. From the comparison of energies of relaxed structures, we have found that after  $V_o^x$  is introduced in the structure, the oxygen-oxygen bond length in  $O_{2o}''$  changes from 1.472 Å to 1.442 Å, which means that  $V_o^x$  makes  $O_{2o}''$  less reactive needing additional energy to break the bond.

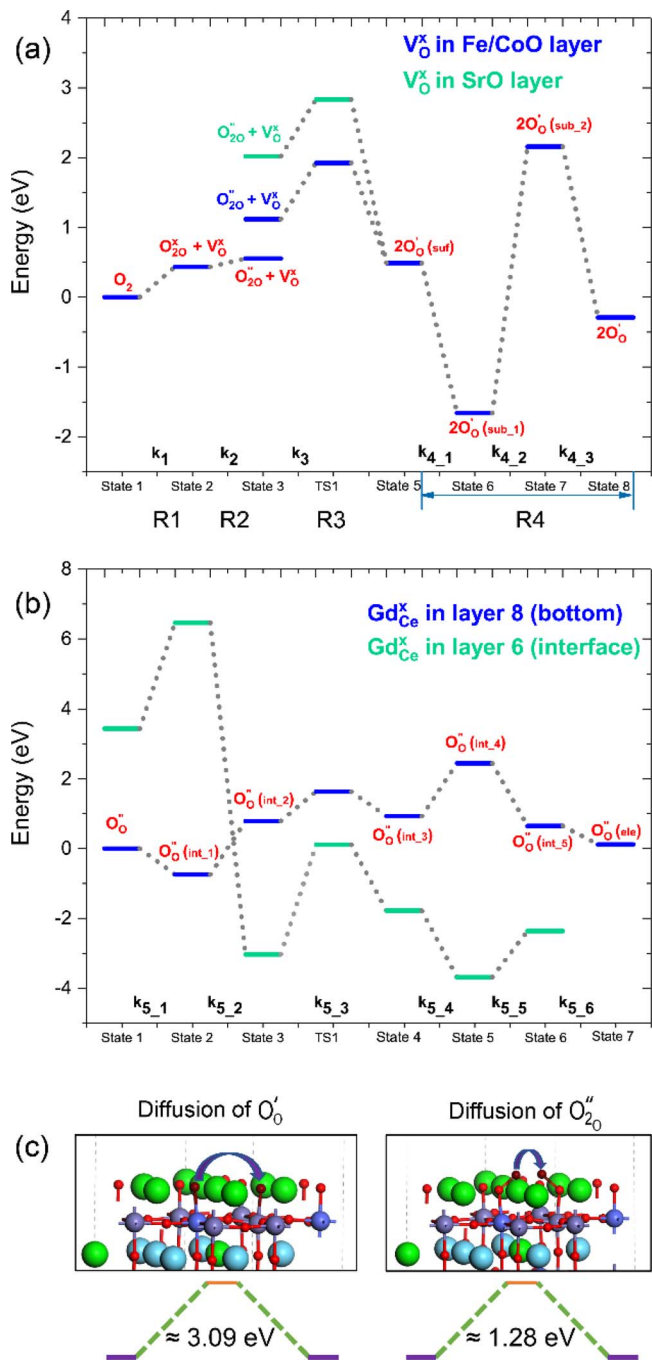
To understand the oxygen adsorption and splitting better, the total density of states (TDOS) and partial density of states (PDOS) of the O(p), Fe(d) and Co(d) are shown in Fig. 6. Oxygen adsorption introduces an acceptor type level close to the Fermi level as seen in Fig. 6b when compared to the TDOS for perfect LSCF crystal (Fig. 6a). This structure then acquires  $2e'$  to form the peroxo species. As seen in the DOS plots, the interaction between the O(p) and Fe(d) and Co(d) orbitals increase leading to increase in covalency of the oxygen atom attached to the surface stretching the O-O bond to 1.472 Å. This tendency of the orbitals indicates a reduction in covalency on the introduction of a  $V_o^x$  (O-O bond length 1.442 Å) and later enhanced covalency after splitting into  $O_o'$ .

Fig. 5b shows the free energy profile for the oxide ion and vacancy exchange at the LSCF/GDC interface,  $R5$ ,  $O_o''(LSCF) + V_o^x(ele) \rightarrow O_o''(ele) + V_o^x(LSCF)$ . Two different configurations for GDC with one Gd atom away from the interface and the other with 2 Gd atoms near the interface have been considered. This reaction contains 6 sub-

steps involving oxide ion migration from bulk LSCF to the interfacial layer, migration within the interfacial layer and the migration from interfacial layer to the bulk electrolyte. Details on these substeps and the definitions of layer indexes are discussed in Section S7 of the Supporting Information. The free energy profile shown in Fig. 5b suggests Layer 5 (as shown in Fig. 3), which is the interfacial layer between SrO (LSCF) and CeO<sub>2</sub> (GDC) layers, is the most stable layer for accommodating oxygen vacancies if the Gd atom is away from the interface. The energy required for oxygen diffusion into the sub-surface of GDC close to a Gd atom at the interface is 3.03 eV whereas it readily enters the sub-surface if the Gd is away from the surface. The energy for diffusion out of GDC to LSCF is also extremely high (9.48 eV) if the Gd atoms are near the interface. For these reasons, Gd atom away from the interface has been chosen for the transport of oxygen across the LSCF/GDC interface. Based on this configuration, the calculations show that the largest barriers come from the migration from layer 4 to layer 5 (0.7 eV) as well as from layer 5 to layer 6 (1.36 eV). Besides, it can be seen from Table S7-1 that the energy barriers to transport at the LSCF/GDC interface are much smaller than those at the LSCF surface.

Fig. 5c shows the free energy profile for diffusion of oxo,  $O_o'$  and peroxo,  $O_{2o}''$  species at the LSCF free surface. The free energy barrier for  $O_o'$  diffusion is very high (3.09 eV), indicating that the diffusion of  $O_o'$  on the LSCF surface is very slow. The free energy barrier for  $O_{2o}''$  diffusion (1.28 eV) is higher than that of the oxide ion ( $O_o''$ ) diffusion in bulk LSCF (about 0.7 eV), and is similar to the calculated  $O_{2o}''$  diffusion on other SrO terminated free surfaces.<sup>21</sup> These results show that the SrO surface layer is inefficient for surface  $O_o'$  and  $O_{2o}''$  species diffusion.

**Influence of concentration variation on free energy barriers.**— The concentration of various species including ions and vacancies affect the energy barrier for various reactions directly as well as indirectly. The direct influence is due to the interaction between lattice ions and defects while the indirect influence is due to electrostatic interactions caused by accumulated charged species. Unlike,  $\Delta G(T)$ , whose values are presented in Table S6-1, expressions for  $\Delta G(C)$



**Figure 5.** (a) Free energy profile for LSCF surface reactions. All energies are with reference to the energy of the  $O_2$  gas. This profile contains reactions R1, R2, R3, and R4. (b) Free energy profile for LSCF/GDC interface reaction, R5. All energies are with reference to the energy of the oxide ion in bulk LSCF. (c) Free energy profile for ion diffusion on the LSCF surface. The brown spheres denote the diffusing oxide ions.

are difficult to obtain theoretically. Therefore, we derived the  $\Delta G(C)$  term for specific reaction steps based on the experimental observations available in the literature.<sup>26,27,46,54</sup>

From Reference 46, the vacancy formation energy of LSCF is related to the oxygen vacancy concentration as:

$$\Delta G_{f,vac} = \Delta G_{f,vac}^{perf} + a \frac{C_{V_O}}{C_{O^{2-}}} \quad [8]$$

where,  $\Delta G_{f,vac}$  is the vacancy formation free energy,  $\Delta G_{f,vac}^{perf}$  is the vacancy formation free energy with no vacancies in the lattice, and

$a$  represents the deviation from the ideal structure. The interactions among defects and lattice ions account for the additional change in free energy.<sup>61,62</sup> The experimental values for  $a$  are presented in Table S7-4. Equation 8 implies that the presence of vacancies in the system makes the formation of further vacancies difficult. As  $C_{V_O}$  in bulk LSCF increases, the vacancies become less stable. Calculations suggest vacancies affect the stability of  $O'_O$  which directly affects their transport and can be explained based on Bader charge analysis. It is observed that after one vacancy is introduced into the bulk LSCF, the average Bader charge of  $O'_O$  changes from 1.231 e to 1.264 e, and the average Bader charge of other cations increases slightly decreasing the covalency and stretching bond lengths. This implies that vacancy introduction increases the electrostatic forces between cations and  $O'_O$  and results in an increase of the energy barriers for migration.

The steps that are affected by the concentration of  $O'_O$  are the reaction step R3 (accounts for the splitting of peroxo species into surface oxo species or combination of surface oxo species into a peroxo species), R4 (accounts for the oxide ion migration between LSCF surface and bulk LSCF), R5 (accounts for the oxide ion transport across the LSCF/GDC interface) and the bulk diffusivity of  $O'_O$  in LSCF. Details on the influence of vacancy concentration on reaction rate constants and diffusivities are presented in Section S8 of the Supporting Information.

Also, as noted in References 26,27, the energy barriers are also indirectly affected by the electrostatic potential difference between the adsorbed oxygen layer and the LSCF surface layer, denoted by  $\chi$ , that exists at the LSCF/gas interface, as shown in Fig. 7.  $\chi$  varies with overpotential. In the SOEC mode, the LSCF surface gets enriched by  $O'_O$ , and the negative charge due to  $O'_O$  enrichment induces an increase of  $\chi$ . In the SOFC mode, the positive charge due to the  $O'_O$  depletion induces the decrease of  $\chi$ . The expressions for  $\Delta G_{k_{R3}^+}(C_{O^-})$ ,  $\Delta G_{k_{R3}^-}(C_{O^-})$  are given by:

$$\begin{aligned} \Delta G_{k_{R3}^+}(C_{O^-}) &= \alpha e \Delta \chi \\ \Delta G_{k_{R3}^-}(C_{O^-}) &= -(1 - \alpha) e \Delta \chi \\ \Delta \chi &= \chi - \chi_{eqi} \end{aligned} \quad [9]$$

where  $e$  is the charge of an electron,  $\alpha$  is the charge transfer coefficient and  $\chi_{eqi}$  is the electrostatic potential at equilibrium. As shown in Fig. 7d,  $d_1$  and  $d_2$  are the distances, the atoms move from initial to transition and transition to final positions respectively, which determine the charge transfer coefficient,  $\alpha = \frac{d_1}{d_1+d_2} \approx \frac{1}{3}$ . The expression for  $\chi$  is:

$$\begin{aligned} \chi &= \frac{F_a C_{O^-}}{C_a p_{surf}} \\ C_a p_{surf} &= \frac{\epsilon_{surf}}{d} \approx \frac{(\epsilon_{air} + \epsilon_{LSCF})}{2d} \end{aligned} \quad [10]$$

where  $C_a p_{surf}$  is the capacitance for surface LSCF,  $d$  is the vertical distance between the uppermost oxygen and the surface layer and is shown in Fig. 7c, and  $\epsilon$  is the permittivity. Here we assume that the surface permittivity value  $\epsilon_{surf}$  is the average of the air permittivity  $\epsilon_{air}$  and the permittivity of LSCF/electrolyte interface  $\epsilon_{LSCF}$ .<sup>63,64</sup> This approximation is consistent with those used in Reference 65. The value for  $\epsilon_{LSCF}$  is listed in Table S6-4.

The electrostatic potential difference,  $\Delta \chi$  is positive in the SOEC mode and negative in SOFC mode because of  $C_{O^-}$  at the LSCF surface which is higher and lower than equilibrium in the respective modes. A positive change in  $\Delta \chi$  helps to lower the reaction barriers in respective directions in each of the modes. As shown in Fig. 7a, in the SOEC mode ( $O'_O$  transfers from the electrolyte into LSCF),  $C_{O^-}$  at the LSCF surface is higher than in equilibrium, and the energy barrier for  $k_{R3}^-$  becomes smaller according to Equation 9, which makes the reaction faster. In the SOFC mode,  $C_{O^-}$  is lower than in equilibrium, and the energy barrier for  $k_{R3}^+$  becomes smaller again.

**Continuum model results.**—The predicted current density-overpotential plot compared to the experimental data is shown in Fig. 8a. A reasonable match is found between the two datasets. The

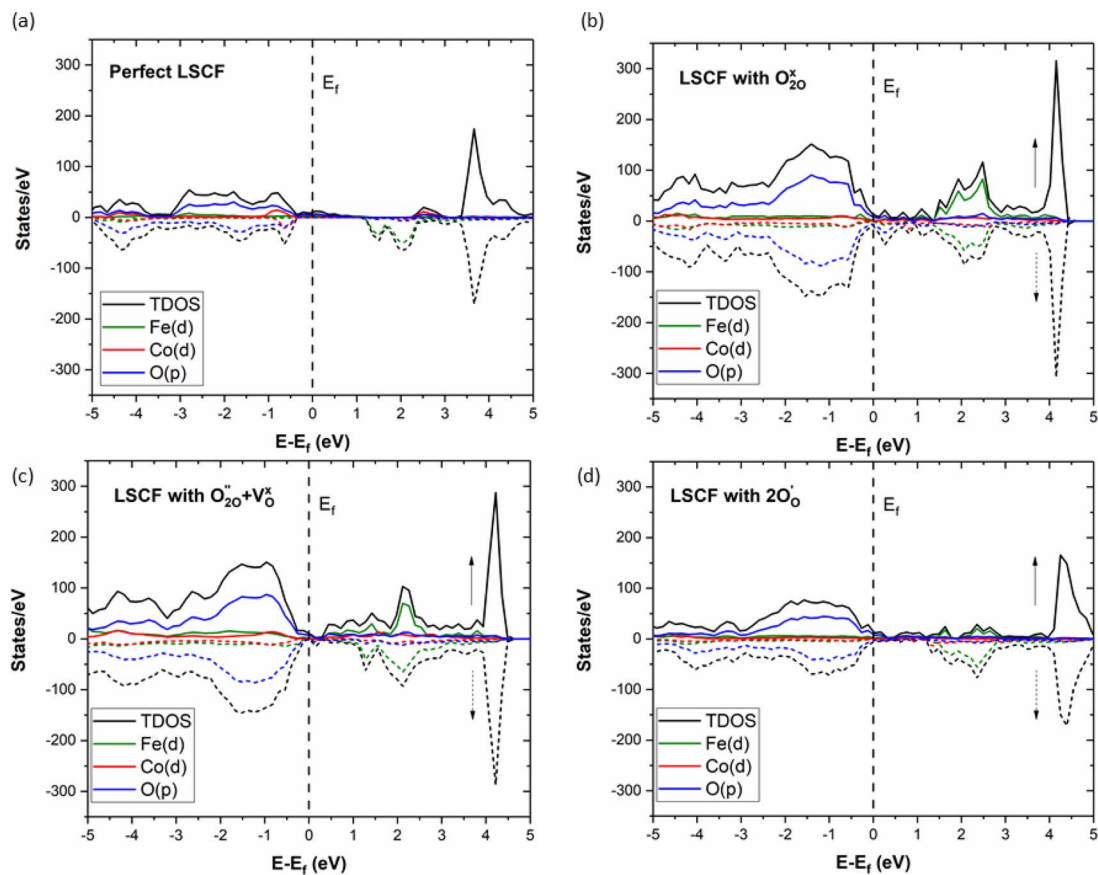


**Figure 6.** The total density of states (TDOS) and projected density of states (PDOS) of O(p), Fe(d) and Co(d) for (a) perfect LSCF crystal; (b) adsorption of O<sub>2</sub> onto LSCF to form excited O<sub>2</sub>O'; (c) attachment of O<sub>2</sub>O' to a nearby vacancy and; (d) LSCF with 2 O'.

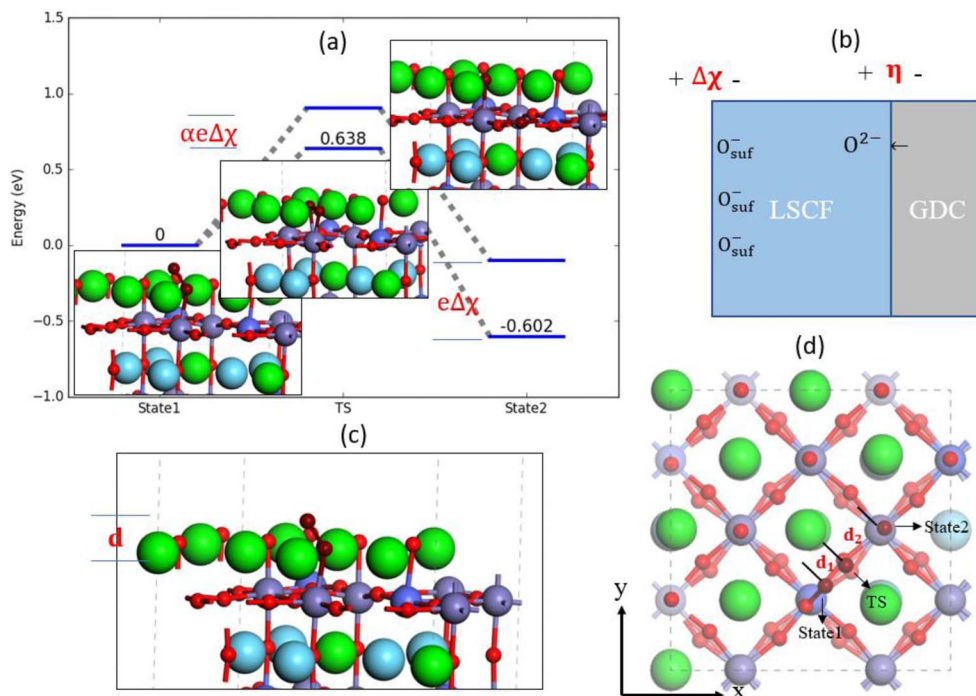


**Figure 7.** Schematic representation of the influence of the electrostatic potential change at the LSCF/gas interface on the reaction rate constants for R3. (a) The energy profile for R3 with and without a positive electrostatic potential change. (b) The mechanism of origin of  $\Delta\chi$ . When O'<sub>2</sub> transfers from the electrolyte into LSCF, LSCF surface gets enriched with O'<sub>2</sub>, and induces the electric potential  $\Delta\chi$ . When O'<sub>2</sub> transfers in the reverse direction,  $\Delta\chi$  will be negative. (c) Side view of the LSCF surface with O'<sub>2</sub>.  $d$  is the vertical distance between the adsorbed oxygen layer and the surface layer. (d) Top view of the R3 sub-process. Brown circles are the initial, transition and final state positions of the moving atom in the reaction.  $d_1$ ,  $d_2$  are the  $x$ - $y$  plane distances moved by atom between the initial and the transition state, and the transition and the final state, respectively.

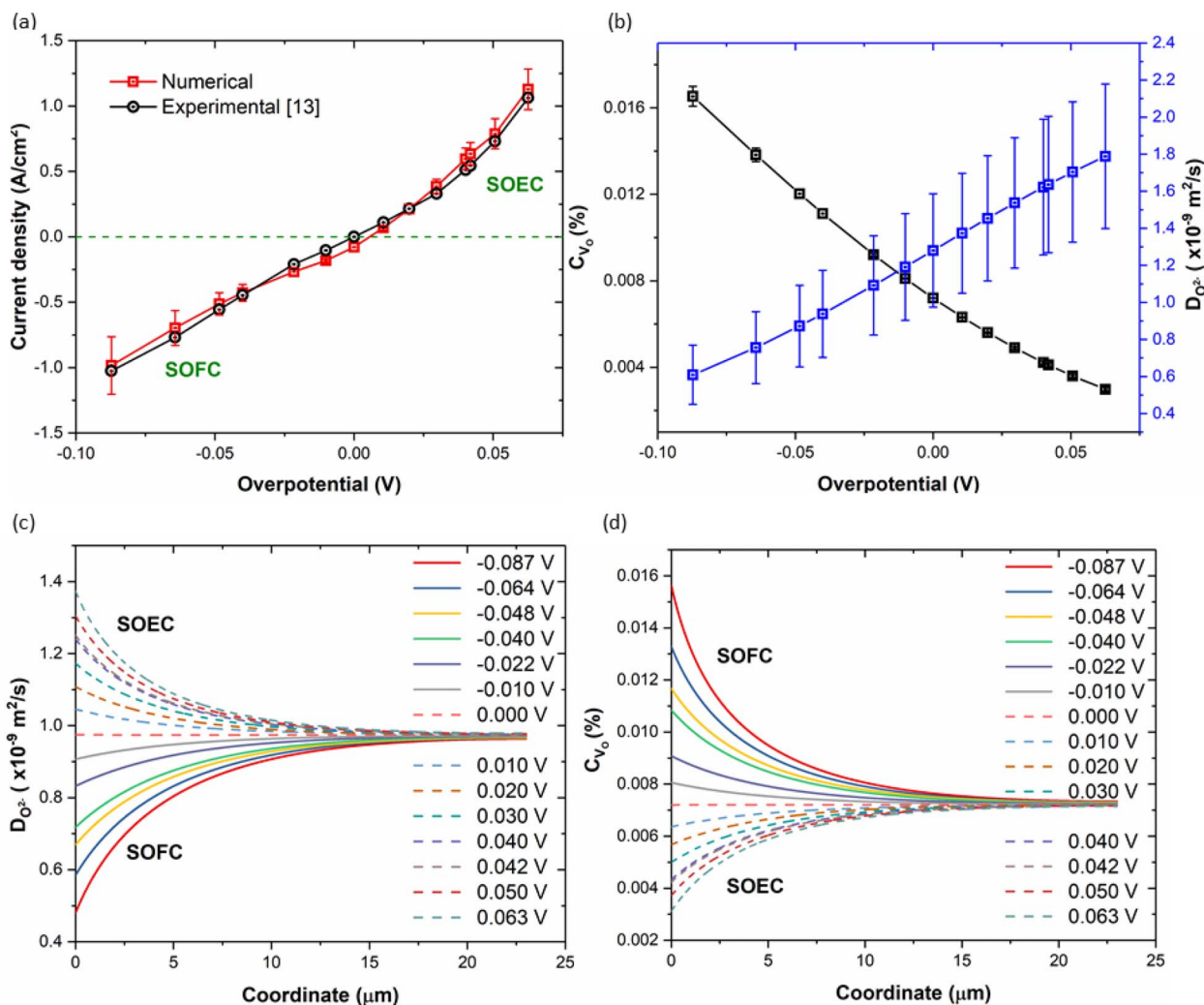


**Figure 8.** Continuum simulation results. (a) Comparison of the numerical and experimental overpotential-current density curves for LSCF based electrode under pressure = 1 atm and temperature = 1073 K. When the current density is less than 0, the cell is working under the fuel cell mode; when the current density is larger than 0, the cell is operating under an electrolysis cell mode. Error bars on the simulation curve come from the uncertainties from published experimental parameters. (b)  $D_{O^{2-}}$  at LSCF/GDC interface and vacancy concentration percentage at LSCF/GDC interface as a function of overpotential. (c)  $D_{O^{2-}}$  in bulk LSCF as a function of z-axis coordinate. Different lines represent different overpotential values, ranging from  $-0.087$  V to  $0.063$  V. (d) Vacancy concentration percentage in bulk LSCF as a function of z-axis coordinate. Different lines represent different overpotential values.

contribution to oxygen exchange through the reaction path across the TPB is neglected in the simulation. Although the current density under SOEC mode is comparable to that under SOFC mode with the same overpotential magnitudes, the governing mechanisms are different. A direct relationship between the concentration of vacancies,  $C_{V_o}$  and diffusivity of oxide ions,  $D_{O^{2-}}$  is seen here. It can be seen from Figs. 8b–8d that the diffusivity of oxide ions in SOEC mode is much higher than that in SOFC mode, and the concentration of oxygen ion vacancies, in SOEC mode is much lower than that in SOFC mode, which is consistent with the literature.<sup>17,66</sup> This may be because oxygen moves from the electrolyte to the electrode in the SOEC mode annihilating vacancies in the electrode, decreasing the  $C_{V_o}$  while oxygen movement from the electrode to electrolyte in SOFC mode creates more vacancies, increasing the  $C_{V_o}$ , which directly influences the  $D_{O^{2-}}$  as has been discussed earlier. The change in  $C_{V_o}$  near the surface may also be caused due to the effect of potential difference on positively charged vacancies. Based on the current density expression  $I = 2F(-D_{O^{2-}} \frac{d}{dz} C_{O^{2-}})$ ,  $I$  is limited by the low concentration gradients,  $\frac{d}{dz} C_{O^{2-}}$  in the SOEC mode, while  $I$  is limited by the low oxide ion diffusivity,  $D_{O^{2-}}$  in SOFC mode.

A sensitivity analysis was performed to analyze the importance of each parameter. The sensitivity of the current density  $S_e$  to other

parameters is given by:

$$S_e = \frac{\partial I/I}{\partial P_a/P_a} \approx \frac{\Delta I/I}{\Delta P_a/P_a} \quad [11]$$

where  $P_a$  is the parameter of interest. As shown in Table II, the current density is sensitive to the reaction rate constants for R3,  $k_{R3}^+$  and  $k_{R3}^-$ , and the oxide ion diffusivity  $D_{O^{2-}}$ . Therefore, it can be concluded that reaction step R3, describing the oxygen-oxygen bond breaking and forming step in SOFC/SOEC, is the critical reaction step, and  $O'_o$  diffusion in bulk LSCF is the critical diffusion step for the system and improving  $k_{R3}^+$ ,  $k_{R3}^-$  and  $D_{O^{2-}}$  can greatly enhance the current density.

Also, neglecting the reaction path across the TPB is a valid assumption. It can be seen from Table S6-2 and Fig. 5c that the surface diffusivities of  $O'_o$  and  $O''_o$  are both much lower compared to bulk  $O'_o$  diffusivity. The low surface diffusivities make the contribution of the reaction path B as shown in Fig. 1 insignificant. It is found that when the concentrations of different species are all within the physical limits:

$$0 \leq C_{O^{2-}}, C_{O^{2-}}, C_{O_2} \leq C_{O^{2-}}^{max}_{surf}$$

**Table II. Sensitivity analysis of various parameters.**

Parameters	Place	$\Delta P_a/P_a$	$S_e (\eta = -0.087)$	$S_e (\eta = 0.063)$
$k_{R1}^+, k_{R1}^-$	LSCF surface	0.05	$\approx 0$	$\approx 0$
$k_{R2}^+, k_{R2}^-$	LSCF surface	0.05	$\approx 0$	$\approx 0$
$k_{R3}^+, k_{R3}^-$	LSCF surface	0.05	[0.466,0.477]	[0.460,0.476]
$k_{R4}^+, k_{R4}^-$	LSCF surface	0.05	[0.009,0.014]	[0.002,0.034]
$k_{R5}^+, k_{R5}^-$	LSCF/GDC interface	0.05	[0.027,0.033]	[0.002,0.009]
$D_{O_2^-}$	Bulk LSCF	0.05	[0.467,0.482]	[0.477,0.481]
$D_{O_2^*}$	LSCF surface	0.05	$\approx 0$	$\approx 0$
$D_{O_2^{2-}}$	LSCF surface	0.05	$\approx 0$	$\approx 0$
$D_{O^-}$	LSCF surface	0.05	$\approx 0$	$\approx 0$

and

$$0 \leq C_{O_2^-} \leq C_{O_2^-}^{max} \quad [12]$$

We have

$$I_{TPB} = -2F_a r_{R6} \leq 0.06 \text{ Acm}^{-2} \quad [13]$$

where  $I_{TPB}$  is the current density across the triple-phase boundary, and its value is much smaller than the experimental current density. Therefore, this reaction path is neglected in this work.

Low  $I_{TPB}$  is attributed to two reasons. First, due to the low surface diffusivities of  $O_{2O}''$  and  $O_O''$ , if  $O_{2O}''$  and  $O_O''$  are far away from the TPB, it is difficult to transport them to the TPB. Therefore, only the  $O_2$  molecules near the TPB can be incorporated into the electrolyte through path B, and this makes this reaction path less likely. On the contrary, the porous electrode provides sufficient surface area for adsorption of oxygen onto the surface and subsequent reactions for oxide ions which can easily transport to the LSCF/GDC interface and into the GDC electrolyte via reaction path A. This makes the reaction rate from path A dominate path B and  $I_{int}$  much larger than  $I_{TPB}$ . Secondly, as shown in Fig. 1, TPB, that can assist in oxygen exchange, only exists at the bottom of the electrode, and the small TPB surface area contributes to the low  $I_{TPB}$ . This TPB area can be greatly enhanced for other electrode structures, such as LSCF-CGO composite electrode,<sup>13</sup> where  $I_{TPB}$  can be higher.

The experimentally observed SrO terminated LSCF surface is not an efficient surface structure for oxidation and evolution reactions. On the one hand,  $C_{O_2^{2-}}$  and  $C_{O_2^-}$  diffuse very slowly on SrO terminated surface making  $I_{TPB}$  very small. On the other hand, the high energy barrier for reaction step R3 on SrO terminated surface from DFT+U calculations results in the slow reaction rate, indicating that SrO terminated surface is not a good catalyst for  $O_{2O}''$  splitting or combination of two  $O_O''$ . This phenomenon has also been reported in a recently published experimental work.<sup>67</sup>

## Conclusions

We have developed a multiscale model combining DFT+U calculations, transition state theory and continuum modeling for the electrochemical processes in LSCF based solid oxide fuel and electrolysis cells. The reactions and overall transport of species at the LSCF based electrode was subdivided into several smaller sub-processes (reaction and transport steps). DFT+U calculations were used to obtain the energy barriers for different reaction and transport steps. Transition state theory was then used to predict the reaction rate constants and diffusivities for each step based on the free energy barriers. Continuum modeling utilized the reaction rate constants, diffusivities, and LSCF microstructure parameters to predict the overpotential-current density plots which were found to be consistent with experimental data. This novel multiscale multi-physics framework making use of data at the atomistic scale to predict electrochemical characteristics in the continuum scale is unique and can easily be applied to other newer oxide systems.

The oxygen exchange at the TPB was found to be negligible as compared to that at the LSCF/GDC interface. Through detailed sensi-

tivity analysis, the chemical reaction involving the splitting of peroxy into oxo species in the SOFC mode/combining of surface oxo into peroxy species in the SOEC mode is found to be the critical and rate-limiting reaction steps. Oxygen vacancies are difficult to transport around Gd atoms at the LSCF/GDC interface and is easier when the Gd atoms are away from the interface. Diffusion of the oxide ion in bulk LSCF is found to be the slowest diffusion step. The direct and indirect influences of concentrations of various species on the reaction barriers were analyzed. It was found that while the vacancy concentrations increase in the SOFC mode leading to reduced diffusivities of oxide ions, the trends are reversed in SOEC mode. SrO terminated LSCF surface is found to be not efficient for oxygen reduction and evolution electrode reactions in SOCs.

## Acknowledgments

This work was supported by the National Science Foundation (USA) under grant # 1545907. This research is part of the Blue Waters sustained-petascale computing project, which is supported by the National Science Foundation (awards OCI-0725070 and ACI-1238993) and the state of Illinois. The authors acknowledge the use of the Taub cluster provided by the Computational Science and Engineering Program at the University of Illinois, and the use of the parallel computing resources Blue Waters provided by the University of Illinois and the National Center for Supercomputing Applications. We thank Yuhang Jing for useful discussions on the DFT calculations as well as the continuum model.

## ORCID

Pikee Priya  <https://orcid.org/0000-0001-5923-7975>

## References

1. L. Bi, S. Boulfrad, and E. Traversa, "Steam electrolysis by solid oxide electrolysis cells (SOECs) with proton-conducting oxides," *Chem. Soc. Rev.*, **43**, 8255 (2014).
2. J. T. S. Irvine, D. Neagu, M. C. Verbraken, C. Chatzichristodoulou, C. Graves, and M. B. Mogensen, "Evolution of the electrochemical interface in high-temperature fuel cells and electrolyzers," *Nat. Energy.*, **1**, 1 (2016).
3. S. B. Adler, "Factors governing oxygen reduction in solid oxide fuel cell cathodes," *Chem. Rev.*, **104**, 4791 (2004).
4. Z. Cheng, J.-H. Wang, Y. Choi, L. Yang, M. C. Lin, and M. Liu, "From Ni-YSZ to sulfur-tolerant anode materials for SOFCs: electrochemical behavior, in situ characterization, modeling, and future perspectives," *Energy Environ. Sci.*, **4**, 4380 (2011).
5. Z. Gao, L. V. Mogni, E. C. Miller, J. G. Railsback, and S. A. Barnett, "A perspective on low-temperature solid oxide fuel cells," *Energy Environ. Sci.*, **9**, 1602 (2016).
6. Y. Zheng, J. Wang, B. Yu, W. Zhang, J. Chen, J. Qiao, and J. Zhang, "A review of high temperature co-electrolysis of H<sub>2</sub>O and CO<sub>2</sub> to produce sustainable fuels using solid oxide electrolysis cells (SOECs): advanced materials and technology," *Chem. Soc. Rev.*, **46**, 1427 (2017).
7. M. A. Laguna-Bercero, "Recent advances in high temperature electrolysis using solid oxide fuel cells: A review," *J. Power Sources.*, **203**, 4 (2012).
8. A. Hauch, S. D. Ebbesen, S. H. Jensen, and M. Mogensen, "Highly efficient high temperature electrolysis," *J. Mater. Chem.*, **18**, 2331 (2008).
9. T. Ishihara, N. Jirathiwathanakul, and H. Zhong, "Intermediate temperature solid oxide electrolysis cell using LaGaO<sub>3</sub> based perovskite electrolyte," *Energy Environ. Sci.*, **3**, 665 (2010).

10. Y. Teraoka, T. Nobunaga, K. Okamoto, N. Miura, and N. Yamazoe, "Influence of constituent metal cations in substituted LaCoO<sub>3</sub> on mixed conductivity and oxygen permeability," *Solid State Ionics*, **48**, 207 (1991).
11. B. C. H. Steele and A. Heinzel, "Materials for fuel-cell technologies," *Nature*, **414**, 345 (2001).
12. A. J. Jacobson, "Materials for solid oxide fuel cells," *Chem. Mater.*, **22**, 660 (2010).
13. J. Laurencin, M. Hubert, K. Couturier, T. Le Bihan, P. Cloetens, F. Lefebvre-Joud, and E. Siebert, "Reactive Mechanisms of LSCF Single-Phase and LSCF-CGO Composite Electrodes Operated in Anodic and Cathodic Polarizations," *Electrochim. Acta.*, **174**, 1299 (2015).
14. H. J. Hwang, J. W. Moon, S. Lee, and E. A. Lee, "Electrochemical performance of LSCF-based composite cathodes for intermediate temperature SOFCs," *J. Power Sources*, **145**, 243 (2005).
15. D. Rembelski, J. P. Viricelle, L. Combemale, and M. Rieu, "Characterization and comparison of different cathode materials for SC-SOFC: LSM, BSCF, SSC, and LSCF," *Fuel Cells*, **12**, 256 (2012).
16. W. Yang, Z. Wang, Z. Wang, X. Yang, C. Xia, R. Peng, X. Wu, and Y. Lu, "Enhanced catalytic activity toward O<sub>2</sub> reduction on Pt-modified La<sub>1-x</sub>Sr<sub>x</sub>Co<sub>1-y</sub>Fe<sub>y</sub>O<sub>3-δ</sub> cathode: A combination study of first-principles calculation and experiment," *ACS Appl. Mater. Interfaces*, **6**, 21051 (2014).
17. B. J. Ingram, J. A. Eastman, K.-C. Chang, S. K. Kim, T. T. Fister, E. Perret, H. You, P. M. Baldo, and P. H. Fuoss, "In situ X-ray studies of oxygen surface exchange behavior in thin film La<sub>0.6</sub>Sr<sub>0.4</sub>Co<sub>0.2</sub>Fe<sub>0.8</sub>O<sub>3-δ</sub>," *Appl. Phys. Lett.*, **101**, 51603 (2012).
18. F. S. Baumann, J. Fleig, G. Cristiani, B. Stuhlhofer, H.-U. Habermeier, and J. Maier, "Quantitative Comparison of Mixed Conducting SOFC Cathode Materials by Means of Thin Film Model Electrodes," *J. Electrochem. Soc.*, **154**, B931 (2007).
19. N. Grunbaum, L. Dessemond, J. Foulletier, F. Prado, L. Moggi, and A. Caneiro, "Rate limiting steps of the porous La<sub>0.6</sub>Sr<sub>0.4</sub>Co<sub>0.8</sub>Fe<sub>0.2</sub>O<sub>3-δ</sub> electrode material," *Solid State Ionics*, **180**, 1448 (2009).
20. T. Akbay, A. Staykov, J. Druce, H. T  llez, T. Ishihara, and J. A. Kilner, "The interaction of molecular oxygen on LaO terminated surfaces of La<sub>2</sub>NiO<sub>4</sub>," *J. Mater. Chem. A*, **4**, 13113 (2016).
21. A. Staykov, H. T  llez, T. Akbay, J. Druce, T. Ishihara, and J. Kilner, "Oxygen Activation and Dissociation on Transition Metal Free Perovskite Surfaces," *Chem. Mater.*, **27**, 8273 (2015).
22. A. Chronos, B. Yildiz, A. Taranc  n, D. Parfitt, and J. A. Kilner, "Oxygen diffusion in solid oxide fuel cell cathode and electrolyte materials: mechanistic insights from atomistic simulations," *Energy Environ. Sci.*, **4**, 2774 (2011).
23. W. Paulus, H. Schober, S. Eibl, M. Johnson, T. Berthier, O. Hernandez, M. Ceretti, M. Plazanet, K. Conder, and C. Lambert, "Lattice dynamics to trigger low temperature oxygen mobility in solid oxide ion conductors," *J. Am. Chem. Soc.*, **130**, 16080 (2008).
24. Z. Wang, R. Peng, W. Zhang, X. Wu, C. Xia, and Y. Lu, "Oxygen reduction and transport on the La<sub>1-x</sub>Sr<sub>x</sub>Co<sub>1-y</sub>Fe<sub>y</sub>O<sub>3-δ</sub> cathode in solid oxide fuel cells: a first-principles study," *J. Mater. Chem. A*, **1**, 12932 (2013).
25. S. B. Adler, "Electrode Kinetics of Porous Mixed-Conducting Oxygen Electrodes," *J. Electrochem. Soc.*, **143**, 3554 (1996).
26. V. Yurkiv, R. Costa, Z. Ilhan, A. Ansar, and W. G. Bessler, "Impedance of the Surface Double Layer of LSCF/CGO Composite Cathodes: An Elementary Kinetic Model," *J. Electrochem. Soc.*, **161**, F480 (2014).
27. J. Fleig, "On the current-voltage characteristics of charge transfer reactions at mixed conducting electrodes on solid electrolytes," *Phys. Chem. Chem. Phys.*, **7**, 2027 (2005).
28. G. Kresse and J. Hafner, "Ab initio molecular dynamics for open-shell transition metals," *Phys. Rev. B*, **48**, 13115 (1993).
29. G. Kresse and J. Furthm  ller, "Efficient iterative schemes for ab initio total-energy calculations using a plane-wave basis set," *Phys. Rev. B*, **54**, 11169 (1996).
30. G. Kresse and J. Furthm  ller, "Efficiency of ab-initio total energy calculations for metals and semiconductors using a plane-wave basis set," *Comput. Mater. Sci.*, **6**, 15 (1996).
31. V. I. Anisimov, J. Zaanen, and O. K. Andersen, "Band theory and Mott insulators: Hubbard U instead of Stoner I," *Phys. Rev. B*, **44**, 943 (1991).
32. S. Dudarev and G. Botton, "Electron-energy-loss spectra and the structural stability of nickel oxide: An LSDA+U study," *Phys. Rev. B - Condens. Matter Mater. Phys.*, **57**, 1505 (1998).
33. A. I. Liechtenstein, V. I. Anisimov, and J. Zaanen, "Density-functional theory and strong interactions: Orbital ordering in Mott-Hubbard insulators," *Phys. Rev. B*, **52**, 5467 (1995).
34. J. P. Perdew, K. Burke, and M. Ernzerhof, "Generalized Gradient Approximation Made Simple," *Phys. Rev. Lett.*, **77**, 3865 (1996).
35. P. E. Bl  chl, "Projector augmented-wave method," *Phys. Rev. B*, **50**, 17953 (1994).
36. G. Kresse and D. Joubert, "From ultrasoft pseudopotentials to the projector augmented-wave method," *Phys. Rev. B*, **59**, 1758 (1999).
37. A. M. Ritzmann, A. B. Mu  oz-Garc  a, M. Pavone, J. A. Keith, and E. A. Carter, "Ab Initio DFT+U analysis of oxygen vacancy formation and migration in La<sub>1-x</sub>Sr<sub>x</sub>FeO<sub>3-δ</sub> (x = 0, 0.25, 0.50)," *Chem. Mater.*, **25**, 3011 (2013).
38. A. M. Ritzmann, M. Pavone, A. B. Mu  oz-Garc  a, J. A. Keith, and E. A. Carter, "Ab initio DFT+U analysis of oxygen transport in LaCoO<sub>3</sub>: the effect of Co<sup>3+</sup> magnetic states," *J. Mater. Chem. A*, **2**, 8060 (2014).
39. A. M. Ritzmann, J. M. Dieterich, and E. A. Carter, "Density functional theory + U analysis of the electronic structure and defect chemistry of LSCF (La<sub>0.5</sub>Sr<sub>0.5</sub>Co<sub>0.25</sub>Fe<sub>0.75</sub>O<sub>3-δ</sub>)," *Phys. Chem. Chem. Phys.*, **18**, 12260 (2016).
40. P. P. Dholabhai, J. B. Adams, P. Crozier, and R. Sharma, "A density functional study of defect migration in gadolinium doped ceria," *Phys. Chem. Chem. Phys.*, **12**, 7904 (2010).
41. G. Henkelman, B. P. Uberuaga, and H. J  nsson, "Climbing image nudged elastic band method for finding saddle points and minimum energy paths," *J. Chem. Phys.*, **113**, 9901 (2000).
42. G. Henkelman, A. Arnaldsson, and H. J  nsson, "A fast and robust algorithm for Bader decomposition of charge density," *Comput. Mater. Sci.*, **36**, 354 (2006).
43. J. D. Pack and H. J. Monkhorst, "Special points for Brillouin-zone integrations," *Phys. Rev. B*, **16**, 1748 (1977).
44. E. Bucher, W. Sitte, G. B. Caraman, V. A. Cherepanov, T. V. Aksenova, and M. V. Ananyev, "Defect equilibria and partial molar properties of (La,Sr)(Co,Fe)O<sub>3-δ</sub>," *Solid State Ionics*, **177**, 3109 (2006).
45. D. Gryaznov, S. Baumann, E. A. Kotomin, and R. Merkle, "Comparison of permeation measurements and hybrid density-functional calculations on oxygen vacancy transport in complex perovskite oxides," *J. Phys. Chem. C*, **118**, 29542 (2014).
46. M. Kuhn, Y. Fukuda, S. Hashimoto, K. Sato, K. Yashiro, and J. Mizusaki, "Oxygen Nonstoichiometry and Thermo-Chemical Stability of Perovskite-Type La<sub>0.6</sub>Sr<sub>0.4</sub>Co<sub>1-y</sub>Fe<sub>y</sub>O<sub>3-δ</sub> (y = 0, 0.2, 0.4, 0.5, 0.6, 0.8, 1) Materials," *J. Electrochem. Soc.*, **160**, F34 (2012).
47. S. R. Bishop, K. L. Duncan, and E. D. Wachsman, "Surface and Bulk Defect Equilibria in Strontium-Doped Lanthanum Cobalt Iron Oxide," *J. Electrochem. Soc.*, **156**, B1242 (2009).
48. A. Jun, S. Yoo, O. H. Gwon, J. Shin, and G. Kim, "Thermodynamic and electrical properties of Ba<sub>0.5</sub>Sr<sub>0.5</sub>Co<sub>0.8</sub>Fe<sub>0.2</sub>O<sub>3-δ</sub> and La<sub>0.6</sub>Sr<sub>0.4</sub>Co<sub>0.2</sub>Fe<sub>0.8</sub>O<sub>3-δ</sub> for intermediate-temperature solid oxide fuel cells," *Electrochim. Acta.*, **89**, 372 (2013).
49. J. Druce, H. T  llez, M. Burriel, M. D. Sharp, L. J. Fawcett, S. N. Cook, D. S. McPhail, T. Ishihara, H. H. Brongersma, and J. A. Kilner, "Surface termination and subsurface restructuring of perovskite-based solid oxide electrode materials," *Energy Environ. Sci.*, **7**, 3593 (2014).
50. K. Chen, N. Li, N. Ai, Y. Cheng, W. D. A. Rickard, and S. P. Jiang, "Polarization-Induced Interface and Sr Segregation in *In Situ* Assembled La<sub>0.6</sub>Sr<sub>0.4</sub>Co<sub>0.2</sub>Fe<sub>0.8</sub>O<sub>3-δ</sub> Electrodes on Y<sub>2</sub>O<sub>3</sub>-ZrO<sub>2</sub> Electrolyte of Solid Oxide Fuel Cells," *ACS Appl. Mater. Interfaces*, **8**, 31729 (2016).
51. R. Kiebach, W. Zhang, M. Chen, K. Norrman, H. J. Wang, J. R. Bowen, R. Barfod, P. V. Hendriksen, and W. Zhang, "Stability of La<sub>0.6</sub>Sr<sub>0.4</sub>Co<sub>0.2</sub>Fe<sub>0.8</sub>O<sub>3</sub>/Ce<sub>0.9</sub>Gd<sub>0.1</sub>O<sub>2</sub> cathodes during sintering and solid oxide fuel cell operation," *J. Power Sources*, **283**, 151 (2015).
52. F. Wang, M. Nishi, M. E. Brito, H. Kishimoto, K. Yamaji, H. Yokokawa, and T. Horita, "Sr and Zr diffusion in LSCF/10GDC/8YSZ triplets for solid oxide fuel cells (SOFCs)," *J. Power Sources*, **258**, 281 (2014).
53. J. A. Lane and J. A. Kilner, "Measuring oxygen diffusion and oxygen surface exchange by conductivity relaxation," *Solid State Ionics*, **137**, 997 (2000).
54. J. A. Lane, S. J. Benson, D. Waller, and J. A. Kilner, "Oxygen transport in La<sub>0.6</sub>Sr<sub>0.4</sub>Co<sub>0.2</sub>Fe<sub>0.8</sub>O<sub>3-δ</sub>," *Solid State Ionics*, **121**, 201 (1999).
55. P. Atkins and J. de Paula, *Atkin's Physical Chemistry*, 10th ed., Oxford University Press, Oxford, UK, 2014.
56. C. T. Campbell and J. R. V. Sellers, "The entropies of adsorbed molecules," *J. Am. Chem. Soc.*, **134**, 18109 (2012).
57. C. T. Campbell and J. R. V. Sellers, "Enthalpies and Entropies of Adsorption on Well-Defined Oxide Surfaces: Experimental Measurements," *Chem. Rev.*, **113**, 4106 (2013).
58. S. Suthirakun, S. C. Ammal, A. B. Mu  oz-Garc  a, G. Xiao, F. Chen, H. C. Zur Loye, E. A. Carter, and A. Heyden, "Theoretical investigation of H<sub>2</sub> oxidation on the Sr<sub>2</sub>Fe<sub>1.5</sub>Mo<sub>0.5</sub>O<sub>6</sub> (001) perovskite surface under anodic solid oxide fuel cell conditions," *J. Am. Chem. Soc.*, **136**, 8374 (2014).
59. H. G. Weller, G. Tabor, H. Jasak, and C. Fureby, "A tensorial approach to computational continuum mechanics using object-oriented techniques," *Comput. Phys.*, **12**, 620 (1998).
60. N. Tsvetkov, Q. Lu, L. Sun, E. J. Crumlin, and B. Yildiz, "Improved chemical and electrochemical stability of perovskite oxides with less reducible cations at the surface," *Nat. Mater.*, **15**, 1010 (2016).
61. J. Mizusaki, M. Hasegawa, K. Yashiro, H. Matsumoto, and T. Kawada, "Nonstoichiometry of the perovskite-type solid solution La<sub>0.9</sub>Ca<sub>0.1</sub>Cr<sub>1-y</sub>Al<sub>y</sub>O<sub>3-δ</sub>," *Solid State Ionics*, **177**, 1925 (2006).
62. Y.-L. Lee, J. Kleis, J. Rossmeisl, Y. Shao-Horn, and D. Morgan, "Prediction of solid oxide fuel cell cathode activity with first-principles descriptors," *Energy Environ. Sci.*, **4**, 3966 (2011).
63. G. M. Rupp, A. Schmid, A. Nening, and J. Fleig, "The Superior Properties of La<sub>0.6</sub>Ba<sub>0.4</sub>CoO<sub>3-δ</sub> Thin Film Electrodes for Oxygen Exchange in Comparison to La<sub>0.6</sub>Sr<sub>0.4</sub>CoO<sub>3-δ</sub>," *J. Electrochem. Soc.*, **163**, F564 (2016).
64. F. S. Baumann, J. Fleig, H. U. Habermeier, and J. Maier, "Impedance spectroscopic study on well-defined (La,Sr)(Co,Fe)O<sub>3-δ</sub> model electrodes," *Solid State Ionics*, **177**, 1071 (2006).
65. A. Donazzi, M. Maestri, and G. Groppi, "A multistep model for the kinetic analysis of the impedance spectra of a novel mixed ionic and electronic conducting cathode," *Electrochim. Acta.*, **222**, 1029 (2016).
66. E. M. Hopper, E. Perret, B. J. Ingram, H. You, K.-C. Chang, P. M. Baldo, P. H. Fuoss, and J. A. Eastman, "Oxygen Exchange in La<sub>0.6</sub>Sr<sub>0.4</sub>Co<sub>0.2</sub>Fe<sub>0.8</sub>O<sub>3-δ</sub> Thin-Film Heterostructures under Applied Electric Potential," *J. Phys. Chem. C*, **119**, 19915 (2015).
67. G. M. Rupp, A. K. Opitz, A. Nening, A. Limbeck, and J. Fleig, "Real-time impedance monitoring of oxygen reduction during surface modification of thin film cathodes," *Nat. Mater.*, **16**, 640 (2017).